

Modelling synchrotron and synchrotron self-Compton emission of gamma-ray burst afterglows from radio to very-high energies

Jagdish C. Joshi^{1,2,3} * and Soebur Razzaque¹ †

¹Centre for Astro-Particle Physics (CAPP) and Department of Physics, University of Johannesburg, PO Box 524, Auckland Park 2006, South Africa

²School of Astronomy and Space Science, Nanjing University, Nanjing 210093, China

³Key laboratory of Modern Astronomy and Astrophysics (Nanjing University), Ministry of Education, Nanjing 210093, China

7 July 2020

ABSTRACT

Synchrotron radiation from a decelerating blastwave is a widely accepted model of radio to X-ray afterglow emission from gamma-ray bursts (GRBs). GeV gamma-ray emission detected by the Fermi Large Area Telescope (LAT) and the duration of which extends beyond the prompt gamma-ray emission phase, is also compatible with broad features of afterglow emission. There is, however, limitations of the simplest version of this pure electron-synchrotron model to explain high-energy photons detected late from the GRB as well as multiwavelength spectral and temporal features. The detection of sub-TeV photons from GRB 190114C can not be modelled using this model. We revisit the synchrotron self-Compton (SSC) emission model from a decelerating blastwave and apply it, together with the synchrotron emission model, to fit multiwavelength data. The model is applied to the GeV bright bursts GRB 090510, GRB 130427A and the MAGIC-detected GRB 190114C. We constrain the afterglow model parameters using the simultaneous fit of the spectral energy distributions at different times and light curves at different frequencies for these bursts. In modelling of the sub-TeV component of GRB 190114C, we find that a larger fraction of shock energy requires in electrons compared to the magnetic field. The same connection cannot be established in the other two GRBs where the SSC component has not been detected.

Key words: Gamma-Ray Bursts : GeV-TeV Component, Multiwavelength Emission

1 INTRODUCTION

Afterglow emission occurs in GRBs after the trigger of a burst which produces the prompt emission. The afterglows are important to understand the radiative processes and the source environments in GRBs, located at cosmological distances. The afterglow emission from GRBs were predicted in radio, optical/UV, X-rays and GeV-TeV bands (Paczynski & Rhoads 1993; Meszaros et al. 1994; Mészáros & Rees 1997; Vietri 1997; Panaitescu & Mészáros 1999; Sari et al. 1998; Chiang & Dermer 1999; Chevalier & Li 2000; Sari & Esin 2001; Granot & Sari 2002; Berger 2014; Kumar & Zhang 2015). These predictions were followed by the discovery in 1997, with X-ray and optical afterglow observations from GRB 970228 (Costa et al. 1997; van Paradijs et al. 1997). Most of the afterglow radiation features are usually explained using the synchrotron model by Sari et al. (1998). More recently the synchrotron models have been successful to interpret Fermi-LAT observations of late GeV emission from GRBs (Kumar & Barniol Duran 2009;

Ghisellini et al. 2010; Razzaque et al. 2010; Pandey et al. 2010); see also Gehrels & Razzaque (2013) for reviews of GeV emission. The recent detection of a sub-TeV spectral component from GRB 190114C and GRB 190829A compliments the expectation of the GRB afterglow models (MAGIC Collaboration et al. 2019a; Abdalla et al. 2019; de Naurois 2019; MAGIC Collaboration et al. 2019b; Zhang 2019).

Physical processes in addition to the synchrotron radiation is required once the photons detected from the afterglow reached above the maximum synchrotron energy limit. The most efficient process to produce GeV-TeV emission is upscattering of synchrotron photons by the same electrons, known as the synchrotron self-Compton (SSC) or inverse-Compton emission. The intensity of the self-Compton signals from the blastwaves, when they interact with the circumburst medium, was predicted by Meszaros & Rees (1994). More detailed calculations were carried out later on by Chiang & Dermer (1999), Panaitescu & Kumar (2000), Zhang & Mészáros (2001), and by Sari & Esin (2001). For the detectability of the SSC component in the afterglow, a higher density; greater than 1 cm^{-3} ; has been estimated by Sari & Esin (2001). The search for this component in GRBs was performed using the Fermi-LAT data and the SSC process was used to ex-

* jjoshi@nuj.edu.cn

† srazzaque@uj.ac.za

plain the delayed GeV component in GRB afterglows (Liu et al. 2013; Panaitescu et al. 2013; Wang et al. 2019). More recently, High Energy Stereoscopic System (HESS) detected sub-TeV emission from GRB 180720B and GRB 190829A with high significance (Abdalla et al. 2019; de Naurois 2019). These detections have renewed modelling activities of these bursts (see, e.g., Fraija et al. 2019a,b,c; Derishev & Piran 2019; Zhang et al. 2019; Ronchi et al. 2020; Chand et al. 2020). In this paper we report on a detailed afterglow synchrotron and SSC model that we have developed and results from its application to the two GeV bright bursts, namely GRB 090510 and GRB 130427A, and to the MAGIC-detected GRB 190114C. The model has been presented for the afterglow emission from the forward shock of an adiabatic blastwave decelerating in a constant density or wind-type environment. We constrain afterglow model parameters using simultaneous fits to the radio to gamma-ray light curves and spectra at different times after the prompt emission.

The outline of this paper is the following. In Section 2, we discuss the dynamics of the blastwave. In Section 3 we discuss the synchrotron emission model and continue with SSC model in Section 4. In Section 5 we discuss absorption of sub-TeV photons in the blastwave and apply our model to GRBs in section 6. We discuss our results in Section 7 and conclude our work in Section 8. The numerical values of the model parameters for different blastwave evolution scenarios are given in the Appendix.

2 BLASTWAVE MODELLING

The GRB event triggers a blastwave, with injected kinetic energy E_k , into the surrounding medium which slows down with time (Blandford & McKee 1976). Considering the event as a point source, it expands with initial Lorentz factor Γ_0 into the surrounding medium. The GRB blastwave at radius r would have the swept-up mass $M_{sw} = 4\pi m_p n r^3/3$, where n is the gas density of the surrounding medium. The deceleration of the blast-wave would be significant when the energy of the swept-up mass is approximately equal to the injected energy into the blastwave. The blastwave moving with Lorentz factor Γ_0 would see the energy of the gas particles blue-shifted by $\Gamma_0 m_p c^2$. This energy would be further boosted by Γ_0 in the observer's frame. We consider half of the energy of the ejecta goes into the blastwave, i.e., $E_k/2 = \Gamma_0^2 M_{sw} c^2$. The deceleration radius r_d is then

$$r_d = \left(\frac{3E_k}{8\pi\Gamma_0^2 m_p c^2 n} \right)^{1/3}. \quad (1)$$

The deceleration time of the blastwave measured by the observer is $t_d = (1+z)r_d/2\Gamma_0^2 c$ (Rees & Meszaros 1992), where z is the redshift, can be expressed as

$$t_d = \left[\frac{3E_k(1+z)^3}{64\pi n m_p c^5 \Gamma_0^8} \right]^{1/3}. \quad (2)$$

The deceleration time in the ISM with constant density $n = n_0 \text{ cm}^{-3}$, $E_k = 10^{55} E_{55} \text{ erg}$ and $\Gamma_0 = 10^{2.5} \Gamma_{2.5}$ (with notation $X = 10^n X_n$) can be written as

$$t_{d,i} = \left[\frac{3E_k(1+z)^3}{64\pi n_0 m_p c^5 \Gamma_0^8} \right]^{1/3} = 33.3 (1+z) n_0^{-1/3} \Gamma_{2.5}^{-8/3} E_{55}^{1/3} \text{ s}. \quad (3)$$

We also consider a wind medium with density profile $n = AR^{-2}$. The mass-loss rate by the progenitor star is $\dot{M}_w =$

$10^{-5} \dot{M}_{-5} M_\odot \text{ yr}^{-1}$, having a wind velocity $v_w = 10^8 v_8 \text{ cm s}^{-1}$. Therefore $A = \dot{M}/(4\pi v_w m_p) = 3.02 \times 10^{35} A_* \text{ cm}^{-1}$, where $A_* \equiv \dot{M}_{-5}/v_8$. The blastwave deceleration time in the wind is then

$$t_{d,w} = \left[\frac{E_k(1+z)}{16\pi A m_p c^3 \Gamma_0^4} \right] = 1.5 (1+z) A_*^{-1} \Gamma_{2.5}^{-4} E_{55} \text{ s}. \quad (4)$$

The radius $R(t)$ of the blastwave or the shock front moves with time t after the deceleration time as (Sari et al. 1998)

$$R(t) = \frac{2\Gamma^2(t) a c t}{1+z}, \quad (5)$$

here $a = 4$ and $a = 7$ represent the expansion scenarios for the adiabatic and radiative blastwave, respectively. Subsequently after the deceleration time, the Lorentz factor of the shocked fluid evolve with time in ISM/wind (i/w) as

$$\Gamma_{ad}(t) = \Gamma_0 \left(\frac{t_{d,i/w}}{4t} \right)^{3/8}; \quad (6)$$

respectively, in the case of an adiabatic expansion. We study the evolution of the blastwave radius R and Lorentz factor Γ in two different scenarios, namely the adiabatic-wind and adiabatic-ISM.

3 SYNCHROTRON EMISSION AND SYNCHROTRON SELF-ABSORPTION

The electrons accelerated at the external shock region radiate away their energy in the amplified magnetic field (see, e.g., Piran 1999; Zhang & Mészáros 2004b). The magnetic field takes away a fraction ϵ_B of the total shock energy, and can be expressed as (all jet-frame quantities are denoted with primes)

$$B'(t) = [32\pi\epsilon_B n(R) m_p c^2]^{1/2} \Gamma(t), \quad (7)$$

where $n(R)$ is the ambient medium density, either wind or ISM. For convenience, we report numerical values of the model parameters for an adiabatic blastwave expansion in these two different scenarios in the Appendix. We discuss shock-accelerated electron spectrum and characteristic breaks therein next.

3.1 Characteristic electron Lorentz factors

We consider that the accelerated electrons follow a power-law spectrum which is defined as $N_e(\gamma'_e) = K \gamma_e'^{-p}$, with spectral index p and normalization $K = (p-1)n' \gamma_m'^{p-1}$. The power-law electron energy distribution to model the GRB afterglows can have a broad spectral index in the range of 1.4-2.8 as found in a set of GRBs by Panaitescu & Kumar (2001). The characteristic Lorentz factor of the accelerated electrons at the forward shock for $p > 2$ is given by (Sari et al. 1998),

$$\gamma'_m(t) = \left[\frac{m_p}{m_e} \epsilon_e \frac{p-2}{p-1} \Gamma(t) \right]; p > 2 \quad (8)$$

The radiation by electrons in the spectrum has two phases of emission called the fast- and slow-cooling. In the fast-cooling, most of the electrons produce the emission efficiently within the dynamic time, while in the slow-cooling, only the high-energy part of the spectrum, above a cooling Lorentz factor γ'_c , cools efficiently. The electron spectrum defined above will be modified in the fast-cooling regime as

$$N_e(\gamma'_e) \propto \begin{cases} \gamma_e'^{-2}, & \gamma'_c \leq \gamma'_e \leq \gamma'_m \\ \gamma_e'^{-p-1}, & \gamma'_e > \gamma'_m, \end{cases} \quad (9)$$

and in the slow-cooling regime as

$$N_e(\gamma'_e) \propto \begin{cases} \gamma_e'^{-p}; & \gamma'_m \leq \gamma'_e \leq \gamma'_c \\ \gamma_e'^{-p-1}, & \gamma'_e > \gamma'_c. \end{cases} \quad (10)$$

The cooling Lorentz factor (γ'_c), can be estimated by comparing the total cooling time $t'_c = 6\pi m_e c / [\sigma_T B'^2 \gamma'_c (1 + Y)]$ with the dynamic or expansion time scale $t'_{dyn} = t\Gamma / (1 + z)$ as

$$\gamma'_c(t) = \left[\frac{6\pi m_e c^2 (1 + z)}{\sigma_T c B'^2(t) t \Gamma(t) (1 + Y)} \right]. \quad (11)$$

Here, σ_T is the Thomson cross-section and $Y \equiv L_{IC}/L_{sy}$ is the Comptonization parameter, which is the ratio between the SSC and synchrotron luminosities. In the case of fast-cooling the Y -parameter can be simply expressed as (Sari & Esin 2001)

$$Y(\text{fast}) = \begin{cases} \epsilon_e/\epsilon_B; \epsilon_e/\epsilon_B \ll 1 \\ \sqrt{\epsilon_e/\epsilon_B}; \epsilon_e/\epsilon_B \gg 1 \end{cases} \quad (12)$$

which is valid for the two different blastwave evolution scenarios. In the case of slow-cooling the situation is more complicated and we solve the relevant equations to obtain

$$Y(\text{slow}) = \sqrt{\epsilon_e/\epsilon_B} \times \begin{cases} (t/t_0^{\text{IC}})^{(2-p)/[2(4-p)]}; & \text{Adiabatic - ISM} \\ (t/t_0^{\text{IC}})^{(2-p)/(4-p)}; & \text{Adiabatic - Wind} \end{cases} \quad (13)$$

The transition time t_0 from the fast- to slow-cooling spectra is defined as $\nu_m(t_0) = \nu_c(t_0)$, and in the presence of SSC cooling of electrons one needs to use the SSC transition time t_0^{IC} (Sari & Esin 2001).

The maximum photon energy emitted by synchrotron cooling is proportional to the saturation Lorentz factor (γ'_s). This is calculated by equating the accelerating time scale $t'_{acc} = \phi \gamma'_e m_e c / [eB'(t)]$, where ϕ^{-1} is the acceleration efficiency for electrons, with the total cooling time t'_c defined earlier as,

$$\gamma'_s(t) = \left[\frac{6\pi e}{\phi \sigma_T B'(t) (1 + Y)} \right]. \quad (14)$$

Typically $\phi = 10$ is assumed and $\phi = 1$ correspond to the maximum efficiency. Again, we report numerical values and parameter dependence of the characteristic Lorentz factors for different fireball evolution scenarios in the Appendix.

3.2 Synchrotron spectra and break frequencies

The synchrotron break frequencies for the electron Lorentz factors γ'_e are related by the expression (Razzaque 2013),

$$h\nu(t) = \frac{3}{2} \frac{B'(t)}{B_Q} m_e c^2 \frac{\Gamma(t)}{1 + z} \gamma_e'^2 \quad (15)$$

where $B_Q = 4.41 \times 10^{13}$ G. Using equation (15) we can calculate the synchrotron break frequencies for the minimum (ν'_m), cooling (ν'_c) and saturation (ν'_s) Lorentz factors γ'_m, γ'_c and γ'_s , respectively. These frequencies in the jet frame are transformed to the observer frame by the relations $\nu = \nu' \Gamma / (1 + z)$. The synchrotron radiation spectrum from these electrons is distributed in particular frequency order, depending on the fast- and slow-cooling (Sari et al. 1998; Granot & Sari 2002; Thomas et al. 2017). The flux of synchrotron

radiation is given in the fast-cooling case as

$$F_{\nu, \text{fast}} = f_{\nu, \text{max}} \begin{cases} \left(\frac{\nu}{\nu_a}\right)^2 \left(\frac{\nu_a}{\nu_c}\right)^{1/3}; & \nu < \nu_a \\ \left(\frac{\nu}{\nu_c}\right)^{1/3}; & \nu_a \leq \nu \leq \nu_c \\ \left(\frac{\nu}{\nu_c}\right)^{-1/2}; & \nu_c < \nu < \nu_m \\ \left(\frac{\nu_m}{\nu_c}\right)^{-1/2} \left(\frac{\nu}{\nu_m}\right)^{-p/2}; & \nu \geq \nu_m, \end{cases} \quad (16)$$

and in the slow-cooling as

$$F_{\nu, \text{slow}} = f_{\nu, \text{max}} \begin{cases} \left(\frac{\nu}{\nu_a}\right)^2 \left(\frac{\nu_a}{\nu_m}\right)^{1/3}; & \nu < \nu_a \\ \left(\frac{\nu}{\nu_m}\right)^{1/3}; & \nu_a \leq \nu \leq \nu_m \\ \left(\frac{\nu}{\nu_m}\right)^{-(p-1)/2}; & \nu_m < \nu < \nu_c \\ \left(\frac{\nu_c}{\nu_m}\right)^{-(p-1)/2} \left(\frac{\nu}{\nu_c}\right)^{-p/2}; & \nu \geq \nu_c. \end{cases} \quad (17)$$

Here $f_{\nu, \text{max}}$ is the maximum synchrotron flux density which is defined as (Sari et al. 1998; Razzaque 2013),

$$f_{\nu, \text{max}} = \frac{N}{4\pi d_L^2} \frac{P(\gamma'_m)}{\nu'_m} \frac{\Gamma^2}{(1 + z)^2}, \quad (18)$$

with the synchrotron power at γ'_m is given by $P(\gamma'_m) = c\sigma_T B'^2 \gamma_m'^2 / 6\pi$ (Rybicki & Lightman 1986). The total number of electrons in the blastwave is given by $N = (4/3)\pi R^3 n$, and the luminosity distance to the source is given by d_L . The time-dependence of the synchrotron flux is governed by the time-dependence of $f_{\nu, \text{max}}$ and of various break frequencies. Depending on a particular frequency band being observed, the break frequencies can pass through that band at different times. Two particularly interesting frequencies are ν_m and ν_c , and the time they appear in the spectrum t_m and t_c , respectively, are reported in the Appendix for the two different blastwave evolution scenarios. The time and frequency evolution of the flux, denoted as $F_\nu \propto t^\alpha \nu^\beta$, give rise to particular relations between α and β for different segments in equations (16) and (17). We report these so-called closure relations (Sari et al. 1998; Granot & Sari 2002; Zhang & Mészáros 2004a) for the synchrotron flux in Table 1. The maximum flux $f_{\nu, \text{max}}$ and various break frequencies are reported in the Appendix. We discuss next the synchrotron-self-absorption frequency.

3.3 Synchrotron self-absorption frequency

The synchrotron spectra in equations (16) and (17) have the lowest frequency break at ν_a , below which the synchrotron spectrum becomes harder by an index $2/3$ due to synchrotron-self-absorption (Rybicki & Lightman 1986). We describe here the derivation of self-absorption frequency ν_a for the blastwave in the circumburst medium. To calculate this we first define the self-absorption coefficient based on (Granot et al. 1999),

$$\alpha'_{\nu'} = \frac{p + 2}{8\pi m_e \nu'^2} \int_{\gamma_m}^{\infty} P'(\gamma'_e) \frac{N_e(\gamma'_e)}{\gamma_e} d\gamma_e. \quad (19)$$

Here the electron distribution $N_e(\gamma_e)$ is independent of the fast- and slow-cooling. From the unmodified electron distribution, defined previously we have

$$N_e(\gamma_e) = n'(p - 1) \gamma_m'^{p-1} \gamma_e^{-p}, \quad (20)$$

where n' is the density of the electrons in the jet frame and is related to the ambient density $n(R)$, with $n' \approx 4\Gamma n(R)$ (Blandford & McKee 1976; Granot et al. 1999) For the electron Lorentz factor γ'_e we can calculate the emitted frequency ν'_{sy} and emitted power $P'(\gamma'_e)$ as (Granot et al. 1999)

$$\nu'_{sy} = \frac{3q_e B'(t) \gamma_e'^2 \sin \alpha}{4\pi m_e c} \quad (21)$$

and

$$P'(\gamma'_e) = \frac{2^{5/3} \pi q_e^3 B'(t) \sin \alpha}{\Gamma(\frac{1}{3}) m_e c^2} \left(\frac{\nu'}{\nu'_{sy}} \right)^{1/3}, \quad (22)$$

respectively. Here, Γ represents the Gamma function. Using equations (19-22) we can derive the expression for the self-absorption coefficient as

$$\alpha'_{\nu'} = \frac{(p+2)(p-1)n'}{8\pi m_e \nu'^{5/3}} \frac{2^{5/3} \pi q_e^3 B'(t) \sin \alpha}{\Gamma(\frac{1}{3}) m_e c^2} \times \left[\frac{4\pi m_e c}{3q_e B'(t) \sin \alpha} \right]^{1/3} \gamma_m^{p-1} \int_{\gamma'_m}^{\infty} \gamma_e^{-(p+5/3)} d\gamma_e. \quad (23)$$

We have further simplified this expression using an average value of $\sin^{3/2} \alpha$, which is equal to $(\sqrt{\pi}/5)\Gamma(1/3)\Gamma(5/6)$, as

$$\alpha'_{\nu'} = 4.72 \times 10^{-10} \left[\frac{(p+2)(p-1)}{(3p+2)\nu'^{5/3}} \right] q_e^{8/3} m_e^{-5/3} \times m_p^{1/3} \epsilon_B^{1/3} \Gamma(t)^{5/3} n(R)^{4/3} \gamma_m^{-5/3}. \quad (24)$$

In the expansion into ISM, $n(R) = n_0$ is a constant density and for wind case it follows the relation $n(R) \propto 1/R^2$ distribution. We derive the absorption coefficients in these two cases as

$$\alpha'_{\nu'}(\text{ISM}) = 925.6 \frac{(p+2)(p-1)}{(3p+2)\nu'^{5/3}} \epsilon_B^{1/3} n_0^{4/3} \gamma_m^{-5/3} \Gamma(t)^{5/3} \quad (25)$$

and

$$\alpha'_{\nu'}(\text{Wind}) = 1.88 \times 10^{50} \frac{(p+2)(p-1)}{(3p+2)\nu'^{5/3}} \times \epsilon_B^{1/3} A_*^{4/3} R(t)^{-8/3} \gamma_m^{-5/3} \Gamma(t)^{5/3}, \quad (26)$$

respectively.

From the above expressions of $\alpha'_{\nu'}$, at the absorption frequency $\nu' = \nu'_a$, the condition that must be satisfied is $\alpha'_{\nu'} R(t)/\Gamma(t) = 1$. Further, following Dermer & Menon (2009) for the slow-cooling case $\gamma'_e = \gamma'_m$ and for the fast-cooling case $\gamma'_e = \gamma'_c$ provides the general expression for the synchrotron-self-absorption frequency as

$$\nu'_{a[s,f]}(\text{ISM}) = 1851.2 \frac{(p+2)(p-1)}{(3p+2)} \times \left[\epsilon_B^{1/3} n_0^{4/3} \gamma_{[m,c]}^{-5/3} \Gamma(t)^{8/3} \frac{act}{1+z} \right]^{3/5} \quad (27)$$

and

$$\nu'_{a[s,f]}(\text{Wind}) = 5.83 \times 10^{49} \frac{(p+2)(p-1)}{(3p+2)} \times \left[\epsilon_B^{1/3} A_*^{4/3} \gamma_{[m,c]}^{-5/3} \Gamma(t)^{-8/3} \left(\frac{act}{1+z} \right)^{-5/3} \right]^{3/5}, \quad (28)$$

respectively, for the ISM and wind medium. The subscripts $[s, f] \rightarrow [m, c]$ refer to the slow- and fast-cooling cases. The self-absorption frequency depends on the spectral index p of the electrons for both the fast- and slow-cooling scenarios, due to their dependence on the minimum Lorentz factor γ'_m . We report numerical values of ν_a in the Appendix for different blastwave evolution scenarios.

4 SYNCHROTRON SELF-COMPTON EMISSION

The inverse-Compton spectrum for the same electrons up-scattering synchrotron photons in the Thomson regime is approxi-

mated by a power-law segment with break frequencies given, following Sari & Esin (2001), by

$$\begin{aligned} \nu_a^{\text{IC}} &\approx 2\gamma_m'^2 \nu_a \\ \nu_m^{\text{IC}} &\approx 2\gamma_m'^2 \nu_m \\ \nu_c^{\text{IC}} &\approx 2\gamma_c'^2 \nu_c \end{aligned} \quad (29)$$

For this component of the spectrum we follow a similar flux distribution as for the synchrotron part with a shift in frequency as defined above. Similar to the maximum synchrotron flux $f_{\nu, \text{max}}$ in equation (18), we define the maximum SSC flux, which is based on the formalism discussed in Zhang & Mészáros (2001), as

$$f_{\nu, \text{max}}^{\text{IC}} = \frac{\nu_m^{\text{sy}} U'_{\text{ph}}}{\nu_m^{\text{IC}} U'_{\text{B}}} f_{\nu, \text{max}}. \quad (30)$$

Here the magnetic energy density is $U'_B = B'^2/8\pi$ and the photon energy density is $U'_{\text{ph}} = (16/3)\sigma_T U'_B \gamma_m'^2 R(t)n(R)$. The SSC component produced in our approximation slightly deviates at higher energies compared to the integrated spectrum of electrons scattered by the seed photons, as discussed in Sari & Esin (2001) and its effects are small.

The fast- and slow-cooling SSC spectra in the Thomson regime follow the same ordering as for the synchrotron spectra. From the flux distribution we can calculate its dependence on the frequency and time, $F_\nu \propto t^\alpha \nu^\beta$, for SSC emission in the two scenarios of blastwave expansions (Panaitescu & Kumar 2000). The temporal and frequency dependence of the fluxes are given in Table 1. The Klein-Nishina effect, however, can become important for SSC emission at very-high energies, which we discuss next.

4.1 Klein-Nishina cutoff energies

Klein-Nishina effect in the IC scattering is important for electrons with Lorentz factor above $\gamma' \approx mc^2/h\nu'$, for scattering photons of frequency ν' in the jet frame. This corresponds to a maximum or cutoff IC photon energy in the Thomson regime as

$$h\nu_{\text{cut}}^{\text{IC}} \approx \frac{m^2 c^4}{h\nu} \frac{\Gamma^2}{(1+z)^2} \quad (31)$$

Photons above this energy are produced inefficiently in the Klein-Nishina regime, where $\nu^{\text{IC}} \approx \gamma'\nu$, and their flux decreases. For the peak synchrotron flux at ν_m , the corresponding cutoff photon energy is

$$\begin{aligned} h\nu_{m, \text{cut}}^{\text{IC}} &\approx 4.1 \left(\frac{p-1}{p-2} \right)^2 (1+z)^{-7/4} \\ &\times \epsilon_{B,-1}^{-1/2} \epsilon_{e,-1}^{-2} n_{0,-5}^{-1/4} E_{55}^{-1/4} t_2^{3/4} \text{ TeV} \end{aligned} \quad (32)$$

for a constant-density environment with density $n_0 = 10^{-5} n_{0,-5} \text{ cm}^{-3}$ and

$$\begin{aligned} h\nu_{m, \text{cut}}^{\text{IC}} &\approx 1.6 \left(\frac{p-1}{p-2} \right)^2 (1+z)^{-2} \\ &\times \epsilon_{B,-1}^{-1/2} \epsilon_{e,-1}^{-2} A_{*-2}^{-1/2} t_2 \text{ TeV} \end{aligned} \quad (33)$$

for the wind environment with the wind parameter $A_* = 10^{-2} A_{*-2}$. Therefore, the cutoff energies increases with time for both cases and can be important during very early afterglow emission. These energies, however, are typically larger than the photon energies, few hundred GeV, at which absorption due to $\gamma\gamma \rightarrow e^\pm$ interactions with the extragalactic background light (EBL) becomes important for cosmological distances (Finke et al. 2010).

Table 1. The closure relations between the temporal index α and spectral index β in various afterglow models for synchrotron and inverse Compton emission with flux distribution $F_\nu \propto t^\alpha \nu^\beta$.

	β	α	$\alpha(\beta)$
Synchrotron emission			
Adiabatic (ISM)		slow cooling	
$\nu < \nu_{a, sy}$	2	1/2	$\beta/4$
$\nu_{a, sy} \leq \nu \leq \nu_{m, sy}$	1/3	1/2	$3\beta/2$
$\nu_{m, sy} < \nu < \nu_{c, sy}$	$-(p-1)/2$	$-3(p-1)/4$	$3\beta/2$
$\nu \geq \nu_{c, sy}$	$-p/2$	$-(3p-2)/4$	$(3\beta+1)/2$
Adiabatic (ISM)		fast cooling	
$\nu < \nu_{a, sy}$	2	1	$\beta/2$
$\nu_{a, sy} \leq \nu \leq \nu_{c, sy}$	1/3	1/6	$\beta/2$
$\nu_{c, sy} < \nu < \nu_{m, sy}$	-1/2	-1/4	$\beta/2$
$\nu \geq \nu_{m, sy}$	$-p/2$	$-(3p-2)/4$	$(3\beta+1)/2$
Adiabatic (wind)		slow cooling	
$\nu < \nu_{a, sy}$	2	1	$\beta/2$
$\nu_{a, sy} \leq \nu \leq \nu_{m, sy}$	1/3	0	$(3\beta-1)/2$
$\nu_{m, sy} < \nu < \nu_{c, sy}$	$-(p-1)/2$	$-(3p-1)/4$	$(3\beta-1)/2$
$\nu \geq \nu_{c, sy}$	$-p/2$	$-(3p-2)/4$	$(3\beta+1)/2$
Adiabatic (wind)		fast cooling	
$\nu < \nu_{a, sy}$	2	2	β
$\nu_{a, sy} \leq \nu \leq \nu_{c, sy}$	1/3	-2/3	$-(\beta+1)/2$
$\nu_{c, sy} < \nu < \nu_{m, sy}$	-1/2	-1/4	$-(\beta+1)/2$
$\nu \geq \nu_{m, sy}$	$-p/2$	$-(3p-2)/4$	$(3\beta+1)/2$
SSC emission			
Adiabatic(ISM)		slow cooling	
$\nu < \nu_{a, ssc}$	2	9/4	9 $\beta/8$
$\nu_{a, ssc} \leq \nu \leq \nu_{m, ssc}$	1/3	1	3 β
$\nu_{m, ssc} < \nu < \nu_{c, ssc}$	$-(p-1)/2$	$-(9p-11)/8$	$(9\beta+1)/4$
$\nu \geq \nu_{c, ssc}$	$-p/2$	$-(9p-10)/8$	$(9\beta+5)/4$
Adiabatic(ISM)		fast cooling	
$\nu < \nu_{a, ssc}$	2	3/4	3 $\beta/8$
$\nu_{a, ssc} \leq \nu \leq \nu_{c, ssc}$	1/3	1/3	β
$\nu_{c, ssc} < \nu < \nu_{m, ssc}$	-1/2	1/8	$-\beta/4$
$\nu \geq \nu_{m, ssc}$	$-p/2$	$-(9p-10)/8$	$(9\beta+5)/4$
Adiabatic (wind)		slow cooling	
$\nu < \nu_{a, ssc}$	2	3/2	3 $\beta/4$
$\nu_{a, ssc} \leq \nu \leq \nu_{m, ssc}$	1/3	-1/3	$-\beta$
$\nu_{m, ssc} < \nu < \nu_{c, ssc}$	$-(p-1)/2$	$-p$	2 $\beta-1$
$\nu \geq \nu_{c, ssc}$	$-p/2$	$-p+1$	2 $\beta+1$
Adiabatic (wind)		fast cooling	
$\nu < \nu_{a, ssc}$	2	11/6	11 $\beta/12$
$\nu_{a, ssc} \leq \nu \leq \nu_{c, ssc}$	1/3	-5/3	-5 β
$\nu_{c, ssc} < \nu < \nu_{m, ssc}$	-1/2	0	$\beta+1/2$
$\nu \geq \nu_{m, ssc}$	$-p/2$	$-p+1$	2 $\beta+1$

5 INTERNAL ABSORPTION IN THE BLASTWAVE

In this section we discuss absorption of gamma-rays within the forward shock due to $\gamma\gamma \rightarrow e^\pm$ interactions with synchrotron photons. The comoving number density of the synchrotron photons with frequency ν can be calculated from the corresponding observed flux

F_ν as

$$n'_\nu = \left(\frac{d_L}{R}\right)^2 \frac{1+z}{\Gamma c} F_\nu \quad (34)$$

As such, the $\gamma\gamma$ optical depth corresponding to that frequency can be calculated in delta-function approximation as

$$\tau_{\gamma\gamma} = \left(\frac{\sigma_T}{5}\right) \frac{n'_\nu R}{\Gamma} \quad (35)$$

This affects the photons of energy

$$E_\gamma = \frac{2m_e^2 c^4 \Gamma^2}{(1+z)^2 h\nu} \quad (36)$$

an estimate, we use $F_\nu = f_{\nu, \max}$ at the minimum synchrotron photon energy $h\nu_m$. These give the opacities in the ISM and wind environments as

$$\begin{aligned} \tau_{\gamma\gamma, \text{ISM}} &= 0.01 (1+z)^{-1/2} n_{0,-5} \epsilon_{B,-1}^{1/2} E_{55}^{1/2} t_2^{1/2} \\ \tau_{\gamma\gamma, \text{wind}} &= 0.8 (1+z)^{1/2} A_{*, -2}^2 \epsilon_{B,-1}^{1/2} E_{55}^{-1/2} t_2^{-1/2} \end{aligned} \quad (37)$$

respectively. The corresponding gamma-ray energies are

$$E_{\gamma, \text{ISM}} = 8.3 \left(\frac{p-1}{p-2}\right)^2 (1+z)^{-7/4} n_{0,-5}^{-1/4} E_{55}^{-1/4} \epsilon_{B,-1}^{-1/2} \epsilon_{e,-1}^{-2} t_2^{3/4} \text{ TeV} \quad (38)$$

for the ISM environment, and

$$E_{\gamma, \text{wind}} = 3.2 \left(\frac{p-1}{p-2}\right)^2 (1+z)^{-2} A_{*, -2}^{-1/2} \epsilon_{B,-1}^{-1/2} \epsilon_{e,-1}^{-2} t_2 \text{ TeV} \quad (39)$$

for the wind environment. As can be seen that the $\gamma\gamma$ opacity in the blastwave is relatively small for substantial attenuation of VHE photons, and again $\gamma\gamma$ attenuation in the EBL is more important (Finke et al. 2010). We have also calculated the $\gamma\gamma$ optical depth, for the full target photon distribution using (Gould & Schröder 1967),

$$\begin{aligned} \tau_{\gamma\gamma}(E_\gamma) &= \frac{R_{\text{in}}}{\Gamma} \pi r_0^2 \left[\frac{m_e c^4 \Gamma}{(1+z) E_\gamma} \right]^2 \\ &\times \int_{\frac{m_e c^4 \Gamma}{(1+z) E_\gamma}}^{(1+z) E_\gamma / \Gamma} \frac{n'(\epsilon')}{\epsilon'^2} \phi[S_0(\epsilon')] d\epsilon', \end{aligned} \quad (40)$$

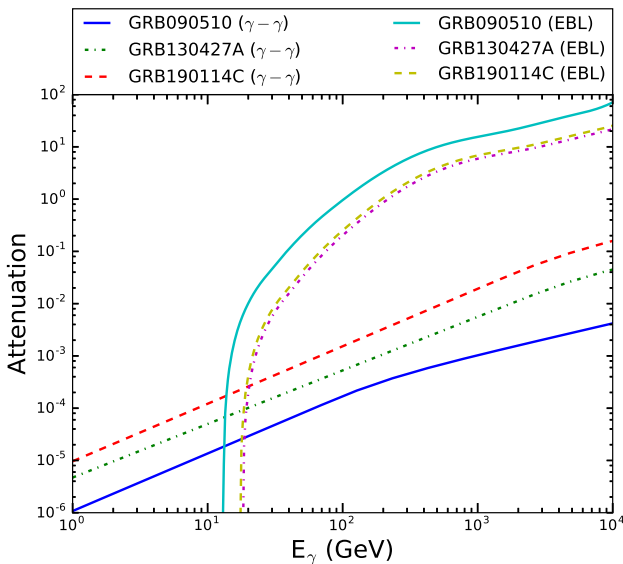
where $\epsilon' = h\nu'$.

6 MODELLING OF BROAD-BAND AFTERGLOW EMISSION

We apply our modelling to GeV-bright bursts, namely the short GRB 090510 and the long GRB 130427A, as well as the recently-detected long GRB 190114C in the sub-TeV energy range. We also explore the the difference in modelling parameters and importance of the sub-TeV component. The parameters used in modelling the afterglow emission in the GRBs below, are given in Table 2. We also show the CTA sensitivity in the SEDs and light curves. In the light curves the sensitivity is plotted at 25 GeV and at 250 GeV. In the SEDs, the CTA sensitivity is shown for a duration of 300-1000 s. In such calculations, a 5σ significance is required in each energy bin and the source flux needs to be few times higher than the background signal. These sensitivities for 25 events in each bin, where 4 bins are taken per decade of energy, is calculated by Funk et al. (2013). These calculations show that the differential

Table 2. The afterglow model parameters from simultaneous interpretation of the SED and light curves.

Parameter	GRB 090510	GRB 130427A	GRB 190114C
E_k (erg)	1×10^{53}	1×10^{55}	3×10^{54}
Γ_0	2000	310	290
t_{dec} (s)	3.6	302.3	56.5
t_0^{IC} (s)	0.2	30.63	12.8
t_{jet} (s)	5000	-	-
A_* (cm^{-1})	-	7.2×10^{-3}	1.6×10^{-2}
n_0 (cm^{-3})	2.2×10^{-5}	-	-
p	2.2	2.05	2.2
ϵ_e	0.2	0.36	0.24
ϵ_B	0.1	1.8×10^{-2}	2.2×10^{-4}
ϕ	1.0	1.0	1.0

**Figure 1.** The $\gamma\gamma \rightarrow e^\pm$ optical depths in the blastwave and in the EBL. The blastwave opacities are calculated for the observed GeV-TeV radiation in the target photon field. These values are estimated at 68 s for GRB 190114C, at 352 s for GRB 130427A, and at 100 s for GRB 090510 where the density of target photons is the maximum for each case. The EBL optical depths for the model by Finke et al. (2010).

flux sensitivity of CTA for 25 GeV gamma-rays is approximately 10^{-9} erg cm^{-2} s^{-1} if the transient source lifetime is considered to be within 10 s. In our work we have used the CTA sensitivity for transients calculated at an elevation angle 70° , which has been retrieved from the CTA website¹.

6.1 Short GRB 090510

The GRB 090510 with a duration of $T_{90} = 0.3 \pm 0.07$ s was observed in the early afterglow phase by the Swift and Fermi satellites (De Pasquale et al. 2010). The redshift of the burst is $z = 0.903 \pm 0.003$ (Rau et al. 2009) and the corresponding luminosity distance is 1.8×10^{28} cm. These observations were modeled using typical synchrotron radiation (De Pasquale et al. 2010;

Ghirlanda et al. 2010; He et al. 2011; Fraija et al. 2016b). A combined electron-proton synchrotron model was used by Razzaque (2010), where the proton component was used to interpret the Fermi-LAT data. A two-component jet model was used by Corsi et al. (2010) to interpret the same data.

Figure 2 shows the data and our model curves for GRB 090510. The optical and X-ray data interpretation favours a constant circumburst environment with a very low density of 2.2×10^{-5} cm^{-3} . The modelling of this source requires slow cooling of the relativistic electrons. The parameters are shown in Table 2 and fast to slow cooling transition occurs at $t_0^{\text{IC}} = 0.2$ s. The no jet break model has surplus of flux in late times, which is corrected using the jet-break feature in this source. In the jet-break, the time dependence of the break frequencies are $\nu_a \propto t^{-1/5}$, $\nu_m \propto t^{-2}$, and $\nu_c \propto t^0$ and the maximum flux goes as $f_{\nu, \text{max}} \propto t^{-1}$. During the jet-break phase the closure relations for slow cooling are $F_\nu \propto \nu^2 t^1$ for $\nu < \nu_a$ and $F_\nu \propto \nu^{1/3} t^{2/3}$ for the regime $\nu_a < \nu < \nu_m$. The late time emission needs a steeper dependence on time and the emission is explained using the regimes $\nu_m < \nu < \nu_c$ where $F_\nu \propto \nu^{-(p-1)/2} t^{1-p}$ and $\nu > \nu_c$ where $F_\nu \propto \nu^{-p/2} t^{1-p}$. The jet-break time is estimated using $t_{\text{jet}} = 5 \times 10^5 (1+z) (E_{55}/n)^{1/3} \theta_{-1}^{8/3}$ s (Sari et al. 1999). We find that the jet-break time is 5000 s, which is in the range of 1.4-5.1 ks, as discussed in Razzaque (2010).

Our modelling confirms the need for very low density ISM medium, as also shown in earlier results by Corsi et al. (2010). The maximum photon energy due to synchrotron emission with our model parameters is 17.5 GeV at 100 s (see the SEDs plotted in Fig. 2) and is adequate to explain the LAT observation. The cutoff SSC photon energy from equation (31) is $h\nu_{m, \text{cut}}^{\text{IC}} \approx 30 t_2^{3/4}$ TeV for the parameters in Table 2. For the same parameters, the opacity in the blastwave $\tau_{\gamma\gamma}$ is plotted in Fig. 1 using equation (40). For the redshift of GRB 090510 the EBL attenuation energy is ~ 100 GeV based on the EBL model by Finke et al. (2010) for which we have also plotted the $\gamma\gamma$ opacity in Fig. 1. Therefore EBL attenuation is more important than internal absorption and KN cutoff. The suppression of the SSC component plotted in Fig. 2 is due to the EBL attenuation.

The breaks in the light curves for 1.8 eV, 1 keV and 15 keV are at $t_m = 2787, 41.2, 6.8$ s, respectively, while for 25 GeV the break is at $t_m^{\text{IC}} = 268$ s. All the light curves after 5000 s follows a break with temporal index $\alpha = 1 - p$, where $p = 2.2$. The dashed vertical gray line shows the deceleration time for blast wave, the point where the emission from the afterglow model starts. We have also shown in the light curve, bottom panel of Figure 2 the rising part before the deceleration time. For slow cooling, which is valid for this case, the rising part is defined as $F_{\nu, s} \propto t^2$ for $\nu < \nu_{a, s}$, $F_{\nu, s} \propto t^3$ for $\nu_{a, s} < \nu < \nu_{m, s}$, $F_{\nu, s} \propto t^3$ for $\nu_{m, s} < \nu < \nu_{c, s}$ and $F_{\nu, s} \propto t^2$ for $\nu > \nu_{c, s}$ (Sari & Piran 1999; Gao et al. 2013). The SSC emission has the temporal dependence for pre-deceleration is $F_{\nu, \text{SSC}} \propto t^3$ for $\nu_{m, \text{SSC}} < \nu < \nu_{c, \text{SSC}}$ and $F_{\nu, \text{SSC}} \propto t$ for $\nu > \nu_{c, \text{SSC}}$. For optical, XRT and BAT energy range we have $F_\nu \propto t^3$ and for the 100 MeV synchrotron flux it is proportional to t^2 , while for SSC emission at 25 GeV, $F_{\nu, \text{SSC}} \propto t^3$.

6.2 Long GRB 130427A

One of the brightest long GRB 130427A with $T_{90} = 276 \pm 5$ s was located at redshift $z = 0.34$ (Levan et al. 2013). The afterglow of GRB 130427A was observed up to 220 ks in radio and optical wavelengths while the X-ray and gamma-ray obser-

¹ <https://www.cta-observatory.org/science/cta-performance>

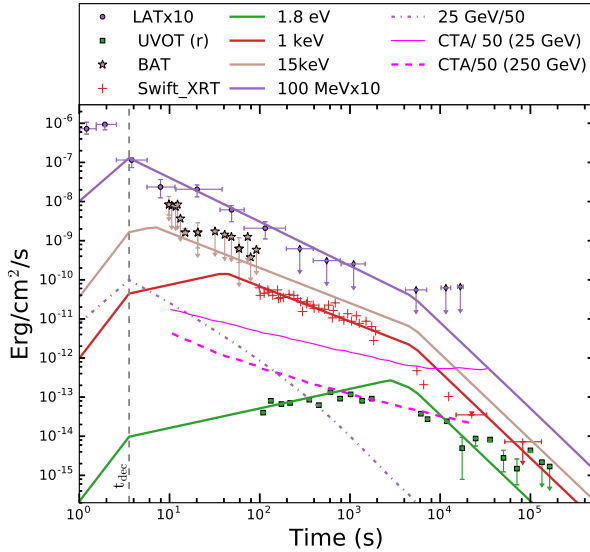
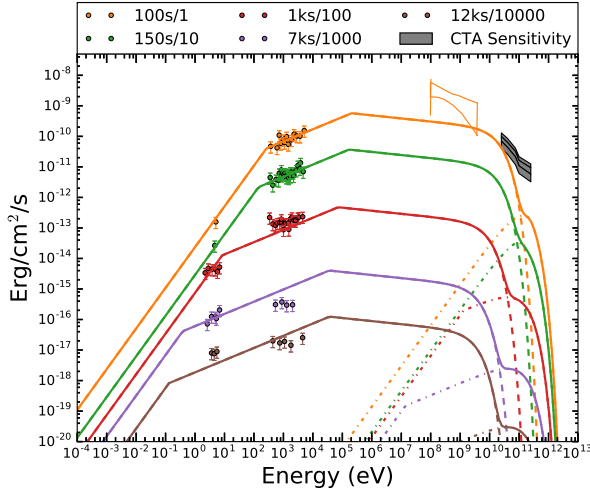


Figure 2. *Top Panel:* The SED of short GRB 090510, where the multiwavelength data are shown for the Swift and Fermi-LAT observations (De Pasquale et al. 2010). *Bottom Panel:* The Swift/BAT (15-350 keV), Swift/UVOT, and Swift/XRT (0.3-10keV), Fermi-LAT (100 MeV-4 GeV) light curves are shown. For the duration of 1.9-5.1 ks, there are no data points in Swift/XRT observation due to Earth occultation. The data points are taken from De Pasquale et al. (2010), SWIFT-XRT database <https://www.swift.ac.uk/analysis/xrt/>. The SED fluxes are scaled by factors 1, 10, 10^2 , 10^3 and 10^4 in decreasing order of time.

vations by Swift-XRT and Fermi-LAT were active upto 1.8 ks (Maselli et al. 2014). A photon of energy 95 GeV was detected at $T_0 + 244$ s and a 32 GeV photon was detected in late time at $T_0 + 34.4$ ks (Ackermann et al. 2014). Its association with a type-Ic supernova (Melandri et al. 2014) provides us further evidence that long GRB 130427A is produced by the collapse of a massive star. The light curves for this source has been modelled for constant density medium (Panaitescu et al. 2013; Maselli et al. 2014; Fan et al. 2013; Liu et al. 2013; Tam et al. 2013) as well as for wind medium (Kouveliotou et al. 2013; Panaitescu et al. 2013; Fraija et al. 2016a). The reverse shock emission features are also used in some models for this burst (Laskar et al. 2013a; Fraija et al. 2016a; Vestrand et al. 2014; Laskar et al. 2013b; Vestrand et al. 2014).

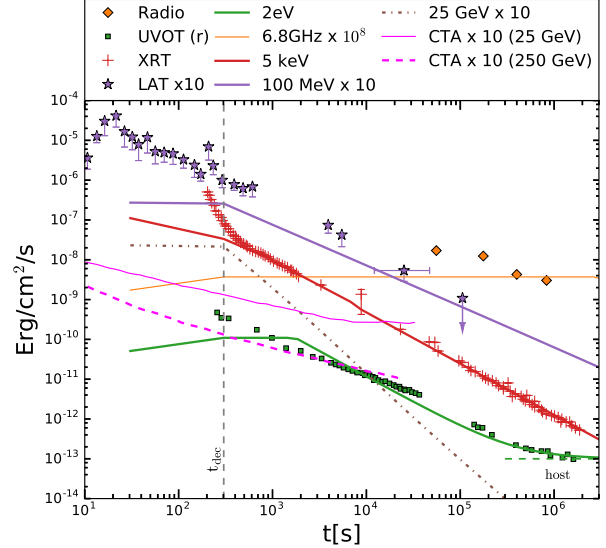
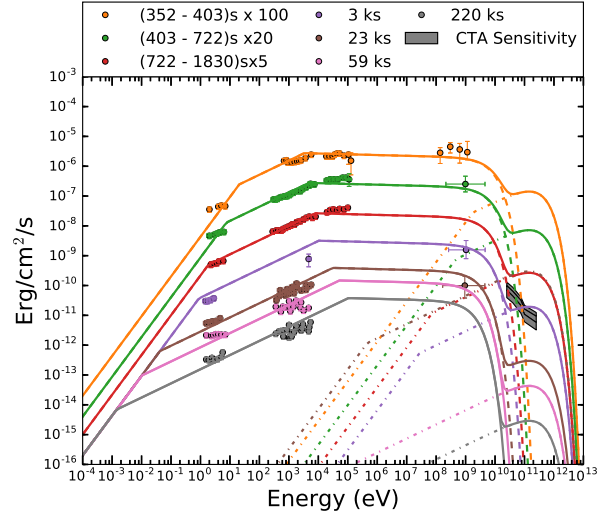


Figure 3. *Top Panel:* The SED of the long GRB 130427A, where in the optical the total contribution of the forward shock and host galaxy is shown. *Bottom Panel:* The light curves in optical to gamma rays for GRB 130427A. The data used in these two plots: Radio 6.8 GHz, UVOT, (0.3-10) keV and LAT (0.1-100) GeV data are taken from Maselli et al. (2014) and from SWIFT-XRT database <https://www.swift.ac.uk/analysis/xrt/>.

The SED and light curves from our modelling for this burst is shown in Fig. 3. We found that a wind environment is preferred in this case. The parameters of our model are reported in Table 2. The early intervals of SED with duration 352-403 s, 403-722 s and 722-1830 s are modelled using times at 352 s, 722 s and 1830 s, respectively. The later SEDs are plotted with mentioned time in the figure legend. We again found that the EBL attenuation is dominant for this burst. The KN cutoff SSC photon energy from equation (31) is $h\nu_{m,cut}^{IC} \approx 80 t_2$ TeV for the parameters obtained for this burst and reported in Table 2. The internal $\gamma\gamma$ opacity is negligible (see Fig. 1). Therefore, we have used a cutoff energy of 300 GeV for the SED at all time in Fig. 3. The breaks in the light curves, for 2 eV is at $t_m \sim 1000$ s, at 5 keV the break is at $t_c = 1005$ s respectively.

The pre-deceleration phase in our light curve, bottom panel of Figure 3 follows the dependence $F_{\nu,s} \propto t^2$ for $\nu < \nu_{a,s}$, $F_{\nu,s} \propto t^{1/3}$ for $\nu_{a,s} < \nu < \nu_{m,s}$, $F_{\nu,s} \propto t^{(1-p)/2}$ for $\nu_{m,s} < \nu < \nu_{c,s}$ and $F_{\nu,s} \propto t^{(2-p)/2}$ for $\nu > \nu_{c,s}$ (Sari & Piran 1999; Gao et al.

2013). The SSC emission has the temporal dependence for pre-deceleration is $F_{\nu,ssc} \propto t^{(1-p)/2}$ for $\nu_{m,ssc} < \nu < \nu_{c,ssc}$ and $F_{\nu,ssc} \propto t^{3/2}$ for $\nu > \nu_{c,ssc}$. For GRB 130427A before deceleration time we have $t^{1/3}$ dependence for 6.8 GHz and 2 eV, and $t^{-0.52}$ for 5 keV and $t^{-0.02}$ for 100 MeV light curve. For the SSC light curve at 25 GeV the dependence is $t^{-0.52}$.

6.3 Long GRB 190114C

The sub-TeV GRB 190114C is located at a redshift $z = 0.42$ (Castro-Tirado et al. 2019) This is the first case of afterglow observation where a sub-TeV component was observed by the MAGIC ground-based Cherenkov telescope (MAGIC Collaboration et al. 2019a,b). The isotropic gamma-ray energy released in this burst was $(2.5 \pm 0.1) \times 10^{53}$ erg (MAGIC Collaboration et al. 2019b) and the burst duration is $T_{90} = 116.4 \pm 2.6$ s for 50-300 keV range (Ajello et al. 2020). It is widely believed that the observed sub-TeV component is the SSC emission from the blastwave.

We have modelled the SEDs and lightcurves of GRB 190114C using synchrotron and SSC emission from an adiabatic blastwave in a wind environment. The sub-TeV components for duration 68-110 s, 110-180 s, 180-360 s and 360-625 s are modelled using times at 68 s, 110 s, 180 s and 360 s, respectively. The SEDs in the duration 68-360 s is well explained by our model. The sub-TeV component can be explained by a larger ratio between the micro-physical parameters $\epsilon_e = 0.22$ and $\epsilon_B = 0.0002$ than the other two bursts we have modelled (see Table 2). For these parameters, the KN cutoff SSC photon energy from equation (31) is $h\nu_{m,cut}^{IC} \approx 100 t_2$ TeV. It can also be seen from Fig. 1 that the internal $\gamma\gamma$ opacity is negligible and very high-energy photons are attenuated in the EBL. To model the SEDs we have used an EBL cutoff energy of 400 GeV at which the EBL opacity is ~ 2 for the model by Finke et al. (2010). In the light curve for this source in Fig. 4, only in optical bands the flux becomes harder for times $10^4 - 5 \times 10^5$ s and it cannot be explained using our one-zone model. The breaks in the light curves, for 2 eV are at $t_m \sim 1000$ s. For GRB 190114C before deceleration time we have $t^{1/3}$ dependence for 18 and 97.5 GHz and 2 eV, and $t^{-0.6}$ for 10 keV and $t^{-0.1}$ for 100 MeV light curve. For the SSC light curve at 25 GeV the dependence is $t^{-0.6}$.

7 DISCUSSION

In our modelling the blastwave is considered to be adiabatic and for GRB 090510 modelling we consider constant density ISM while for other two cases the medium is taken to be wind medium. In case of GRB 090510 our model parameters $\epsilon_e = 0.2$, $n_0 = 2.2 \times 10^{-5}$ matches with the earlier modelling of this source (Fraija et al. 2016b) but we need the parameter ϵ_B larger by a factor 10 in our case. The large value of $\Gamma_0 = 2000$ is needed to optimize the deceleration time and is also used in modelling of this burst by Ghirlanda et al. (2010). We found synchrotron dominance in GRB 090510 compared to the SSC signal and the jet-break features are observed at 5 ks.

The initial Lorentz factor $\Gamma_0 = 310$ used for GRB 130427A is slightly lower compared to (Fraija et al. 2016a) and lower compared to (Panaitescu et al. 2013). The fraction of energy in electrons is similar to (Fraija et al. 2016a) but we use higher fraction of energy in magnetic field and larger value of isotropic kinetic energy into the blastwave. In the optical emission for time larger than

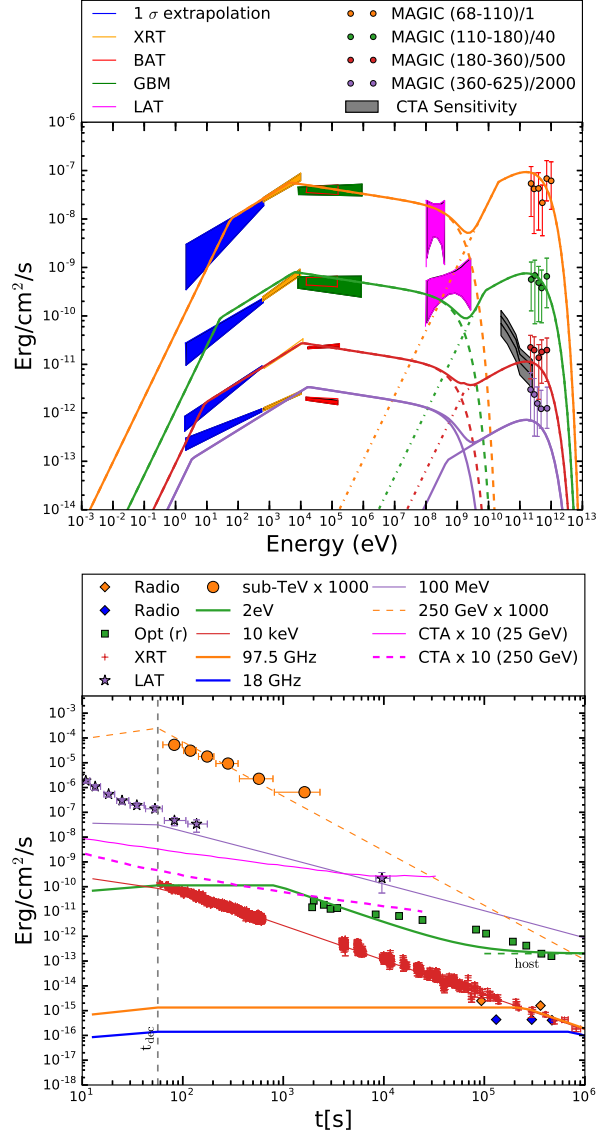


Figure 4. *Top Panel:* The SED of the long GRB 190114C and we have shown our model fit to MAGIC sub TeV data. *Bottom Panel:* The data used in these two plots: Radio 18 and 97.5 GHz, UVOT, XRT (0.3-10) keV, BAT (15-150) keV, GBM (10 - 10^4) keV, LAT (0.1-100) GeV are taken from (Ajello et al. 2020), MAGIC Collaboration et al. (2019b) and SWIFT-XRT database <https://www.swift.ac.uk/analysis/xrt/>.

3×10^5 s, we have added the host galaxy emission in bottom panel of Figure 3.

For this object also we have used an initial Lorentz factor $\Gamma_0 = 290$, which is useful for producing the afterglow emission above 55 s. The sub-TeV component in GRB 190114C has very similar flux levels as in X-rays. The interpretation of the X-ray and sub-TeV emission requires approximately 1000 times larger shock energy distribution in electrons compared to the magnetic field. The same scenario can-not be established for other two bright GRBs, modelled in this work. For the duration in between $10^4 - 10^5$ s the spectrum of optical photons in GRB 190114C is harder and might be due to refreshed shock (Rees & Mészáros 1998). Above 10^5 s the host galaxy emission is added for the interpretation of the optical emission in bottom panel of Figure 4.

In all three GRBs, we found that the internal $\gamma\gamma$ absorption in

the blastwave is not important to the extent of the energy allowed by the EBL. In principle, gamma rays absorbed in the EBL can initiate a cascade and secondary contributions to the overall emission can be important if the intergalactic magnetic field is $\lesssim 10^{-19}$ G (see, e.g., Razzaque et al. 2004; Ando 2004; Murase et al. 2007). We do not, however, discuss this here. We also found that the SSC emission in the Thomson regime can be used to model the sub-TeV observations of GRB 190114C. Derishev & Piran (2019) also found that Thomson scattering is favoured in compared to the Klein-Nishina effect for this burst. A future study will include variations in the Compton Y parameter in the KN range and its implications to understand the sub-TeV emissions in GRBs (Nakar et al. 2009; Wang et al. 2010; Fraija et al. 2020). The analytical approximations used for estimation of SSC flux in this work, will have minute deviation in SSC flux above ν_m^{IC} (Sari & Esin 2001) and these effects are not considered in this work.

8 CONCLUSION

In conclusions, our synchrotron-SSC modelling proves to be useful in fitting multiwavelength afterglow data from long and short GRBs, including VHE data. Modelling these data sheds light on the GRB blastwave models and physical parameters involved in radio to VHE gamma-ray emission. The predicted SSC emission is less dominant in GRB 090510 and significant for GRB 130427A. The detection of this component in GRB 190114C is important to study the shock energy distributions in electrons and magnetic fields, and the environment surrounding the GRBs. In particular, detection of the VHE emission requires much higher energy density in the shocked electrons than in the magnetic fields. The frequent detection of TeV component in GRB afterglows by upcoming CTA and the Large High Altitude Air Shower Observatory (LHASSO) (Cherenkov Telescope Array Consortium et al. 2019; Bai et al. 2019) will enrich GRB afterglow models.

9 ACKNOWLEDGEMENTS

The research work of J.C.J. was supported by a GES fellowship at the University of Johannesburg, where most part of the work is completed. We are thankful to X.-Y. Wang and N. Fraija and S. B. Pandey for reading the manuscript and comments, R. J. Britto for providing the python script for the optical depth calculation and M. Arimoto for helpful comments. S.R. acknowledges support from the National Research Foundation (South Africa) with Grant No. 111749 (CPRR).

REFERENCES

Abdalla H. et al., 2019, *Nature*, 575, 464
 Ackermann M. et al., 2014, *Science*, 343, 42
 Ajello M. et al., 2020, *ApJ*, 890, 9
 Ando S., 2004, *MNRAS*, 354, 414
 Bai X. et al., 2019, arXiv e-prints, arXiv:1905.02773
 Berger E., 2014, *ARA&A*, 52, 43
 Blandford R. D., McKee C. F., 1976, *Physics of Fluids*, 19, 1130
 Castro-Tirado A. J. et al., 2019, *GRB Coordinates Network*, 23708, 1
 Chand V. et al., 2020, arXiv e-prints, arXiv:2001.00648
 Cherenkov Telescope Array Consortium et al., 2019, *Science with the Cherenkov Telescope Array*
 Chevalier R. A., Li Z.-Y., 2000, *ApJ*, 536, 195
 Chiang J., Dermer C. D., 1999, *ApJ*, 512, 699

Corsi A., Guetta D., Piro L., 2010, *ApJ*, 720, 1008
 Costa E. et al., 1997, *Nature*, 387, 783
 de Naurois M., 2019, *The Astronomer's Telegram*, 13052, 1
 De Pasquale M. et al., 2010, *ApJ*, 709, L146
 Derishev E., Piran T., 2019, *ApJ*, 880, L27
 Dermer C. D., Menon G., 2009, *High Energy Radiation from Black Holes: Gamma Rays, Cosmic Rays, and Neutrinos*, Princeton University Press
 Fan Y.-Z. et al., 2013, *ApJ*, 776, 95
 Finke J. D., Razzaque S., Dermer C. D., 2010, *ApJ*, 712, 238
 Fraija N., Barniol Duran R., Dichiarà S., Beniamini P., 2019a, *ApJ*, 883, 162
 Fraija N., Dichiarà S., Pedreira A. C. C. d. E. S., Galvan-Gamez A., Becerra R. L., Barniol Duran R., Zhang B. B., 2019b, *ApJ*, 879, L26
 Fraija N. et al., 2019c, *ApJ*, 885, 29
 Fraija N., Lee W., Veres P., 2016a, *ApJ*, 818, 190
 Fraija N., Lee W. H., Veres P., Barniol Duran R., 2016b, *ApJ*, 831, 22
 Fraija N., Veres P., Beniamini P., Galvan-Gamez A., Metzger B. D., Barniol Duran R., Becerra R. L., 2020, arXiv e-prints, arXiv:2003.11252
 Funk S., Hinton J. A., CTA Consortium, 2013, *Astroparticle Physics*, 43, 348
 Gao H., Lei W.-H., Zou Y.-C., Wu X.-F., Zhang B., 2013, *New A Rev.*, 57, 141
 Gehrels N., Razzaque S., 2013, *Frontiers of Physics*, 8, 661
 Ghirlanda G., Ghisellini G., Nava L., 2010, *A&A*, 510, L7
 Ghisellini G., Ghirlanda G., Nava L., Celotti A., 2010, *MNRAS*, 403, 926
 Gould R. J., Schröder G. P., 1967, *Phys. Rev.*, 155, 1404
 Granot J., Piran T., Sari R., 1999, *ApJ*, 527, 236
 Granot J., Sari R., 2002, *ApJ*, 568, 820
 He H.-N., Wu X.-F., Toma K., Wang X.-Y., Mészáros P., 2011, *ApJ*, 733, 22
 Kouveliotou C. et al., 2013, *ApJ*, 779, L1
 Kumar P., Barniol Duran R., 2009, *MNRAS*, 400, L75
 Kumar P., Zhang B., 2015, *Phys. Rep.*, 561, 1
 Laskar T. et al., 2013a, *ApJ*, 776, 119
 Laskar T. et al., 2013b, *ApJ*, 776, 119
 Levan A. J., Cenko S. B., Perley D. A., Tanvir N. R., 2013, *GRB Coordinates Network*, 14455, 1
 Liu R.-Y., Wang X.-Y., Wu X.-F., 2013, *ApJ*, 773, L20
 MAGIC Collaboration et al., 2019a, *Nature*, 575, 455
 MAGIC Collaboration et al., 2019b, *Nature*, 575, 459
 Maselli A. et al., 2014, *Science*, 343, 48
 Melandri A. et al., 2014, *A&A*, 567, A29
 Meszaros P., Rees M. J., 1994, *MNRAS*, 269, L41
 Mészáros P., Rees M. J., 1997, *ApJ*, 476, 232
 Meszaros P., Rees M. J., Papathanassiou H., 1994, *ApJ*, 432, 181
 Murase K., Asano K., Nagataki S., 2007, *ApJ*, 671, 1886
 Nakar E., Ando S., Sari R., 2009, *ApJ*, 703, 675
 Paczynski B., Rhoads J. E., 1993, *ApJ*, 418, L5
 Panaitescu A., Kumar P., 2000, *ApJ*, 543, 66
 Panaitescu A., Kumar P., 2001, *ApJ*, 560, L49
 Panaitescu A., Mészáros P., 1999, *ApJ*, 526, 707
 Panaitescu A., Vestrand W. T., Woźniak P., 2013, *MNRAS*, 436, 3106
 Pandey S. B. et al., 2010, *ApJ*, 714, 799
 Piran T., 1999, *Phys. Rep.*, 314, 575
 Rau A., McBreen S., Kruehler T., 2009, *GRB Coordinates Network*, 9353, 1
 Razzaque S., 2010, *ApJ*, 724, L109
 Razzaque S., 2013, *Phys. Rev. D*, 88, 103003
 Razzaque S., Dermer C. D., Finke J. D., 2010, *The Open Astronomy Journal*, 3, 150
 Razzaque S., Mészáros P., Zhang B., 2004, *ApJ*, 613, 1072
 Rees M. J., Meszaros P., 1992, *MNRAS*, 258, 41P
 Rees M. J., Mészáros P., 1998, *ApJ*, 496, L1
 Ronchi M. et al., 2020, *A&A*, 636, A55
 Rybicki G. B., Lightman A. P., 1986, *Radiative Processes in Astrophysics*, p. 400
 Sari R., Esin A. A., 2001, *ApJ*, 548, 787
 Sari R., Piran T., 1999, *ApJ*, 520, 641

- Sari R., Piran T., Halpern J. P., 1999, ApJ, 519, L17
Sari R., Piran T., Narayan R., 1998, ApJ, 497, L17
Tam P.-H. T., Tang Q.-W., Hou S.-J., Liu R.-Y., Wang X.-Y., 2013, ApJ, 771, L13
Thomas J. K., Moharana R., Razzaque S., 2017, Phys. Rev. D, 96, 103004
van Paradijs J. et al., 1997, Nature, 386, 686
Vestrand W. T. et al., 2014, Science, 343, 38
Vietri M., 1997, ApJ, 478, L9
Wang X.-Y., He H.-N., Li Z., Wu X.-F., Dai Z.-G., 2010, ApJ, 712, 1232
Wang X.-Y., Liu R.-Y., Zhang H.-M., Xi S.-Q., Zhang B., 2019, arXiv e-prints, arXiv:1905.11312
Zhang B., 2019, Nature, 575, 448
Zhang B., Mészáros P., 2001, ApJ, 559, 110
Zhang B., Mészáros P., 2004a, International Journal of Modern Physics A, 19, 2385
Zhang B., Mészáros P., 2004b, International Journal of Modern Physics A, 19, 2385
Zhang H., Christie I., Petropoulou M., Rueda-Becerril J. M., Giannios D., 2019, arXiv e-prints, arXiv:1910.14049

APPENDIX

Below we give numerical expressions for the blastwave evolution parameters, synchrotron parameters and break frequencies, and SSC parameters and break frequencies. These values are described for the adiabatic blastwaves when they propagate in the constant density medium (ISM) or in a wind-type environment. Here $d_{28} = d_L/10^{28}$ cm and $t_2 = t/100$ s and $\nu_{eV} = \nu/1\text{eV}$.

Adiabatic blastwave in the constant density medium

$$\Gamma = 124.49 (1+z)^{3/8} n_0^{-1/8} E_{55}^{1/8} t_2^{-3/8} \quad (\text{A-1})$$

$$R = 3.72 \times 10^{17} (1+z)^{-1/4} n_0^{-1/4} E_{55}^{1/4} t_2^{1/4} \text{ cm} \quad (\text{A-2})$$

$$B' = 15.3 (1+z)^{3/8} \epsilon_{B,-1}^{1/2} n_0^{3/8} E_{55}^{1/8} t_2^{-3/8} \text{ G} \quad (\text{A-3})$$

$$\gamma'_m = 2.3 \times 10^4 \left(\frac{p-2}{p-1} \right) (1+z)^{3/8} \epsilon_{e,-1} n_0^{-1/8} E_{55}^{1/8} t_2^{-3/8} \quad (\text{A-4})$$

$$\gamma'_c = 265.33 (1+z)^{-1/8} \epsilon_{B,-1}^{-1} n_0^{-5/8} E_{55}^{-3/8} t_2^{1/8} (1+Y)^{-1} \quad (\text{A-5})$$

$$\gamma'_s = 9.42 \times 10^6 (1+z)^{-3/16} \epsilon_{B,-1}^{-1/4} n_0^{-3/16} \phi_1^{-1/2} E_{55}^{-1/16} t_2^{3/16} (1+Y)^{-1/2} \quad (\text{A-6})$$

$$h\nu_{a,\text{fast}} = 1.77 \times 10^{-2} \left[\frac{(p+2)(p-1)}{(3p+2)} \right]^{3/5} (1+z)^{-1/2} \epsilon_{B,-1}^{6/5} n_0^{11/10} E_{55}^{7/10} t_2^{-1/2} (1+Y) \text{ eV} \quad (\text{A-7})$$

$$h\nu_{a,\text{slow}} = 2.1 \times 10^{-4} \frac{(p+2)^{3/5} (p-1)^{8/5}}{(3p+2)^{3/5} (p-2)} (1+z)^{-1} \epsilon_{B,-1}^{1/5} \epsilon_{e,-1}^{-1} n_0^{3/5} E_{55}^{1/5} \text{ eV} \quad (\text{A-8})$$

$$h\nu_c = 2.33 (1+z)^{-1/2} \epsilon_{B,-1}^{-3/2} n_0^{-1} E_{55}^{-1/2} t_2^{-1/2} (1+Y)^{-2} \text{ eV} \quad (\text{A-9})$$

$$h\nu_m = 17.3 \left(\frac{p-2}{p-1} \right)^2 (1+z)^{1/2} \epsilon_{B,-1}^{1/2} \epsilon_{e,-1}^2 E_{55}^{1/2} t_2^{-3/2} \text{ keV} \quad (\text{A-10})$$

$$h\nu_s = 2.94 (1+z)^{-5/8} \phi_1^{-1} n_0^{-1/8} E_{55}^{1/8} t_2^{-3/8} (1+Y)^{-1} \text{ GeV} \quad (\text{A-11})$$

The above set of frequencies builds-up the spectral energy distribution for synchrotron emission. For these set of frequencies we also calculate the time when they will appear in the spectrum. We list two most frequent time breaks, t_c and t_m ,

$$t_c = 5.43 \times 10^2 (1+z)^{-1} \epsilon_{B,-1}^{-3} n_0^{-2} E_{55}^{-1} (1+Y)^{-4} \nu_{c,\text{eV}}^{-2} \text{ s} \quad (\text{A-12})$$

$$t_m = 6.69 \times 10^4 \left(\frac{p-2}{p-1} \right)^{4/3} (1+z)^{1/3} \epsilon_{B,-1}^{1/3} \epsilon_{e,-1}^{4/3} E_{55}^{1/3} \nu_{m,\text{eV}}^{-2/3} \text{ s} \quad (\text{A-13})$$

The synchrotron transition time for the fast to slow cooling is calculated for the time when ν_m and ν_c coincides, i.e. $\nu_m(t_0) = \nu_c(t_0)$, The synchrotron and effective inverse-Compton cooling times are given by,

$$t_0 = 7.41 \times 10^5 \left(\frac{p-2}{p-1} \right)^2 (1+z) \epsilon_{B,-1}^2 \epsilon_{e,-1}^2 n_0 E_{55} \text{ s} \quad (\text{A-14})$$

$$t_0^{\text{IC}} = 7.41 \times 10^5 \left(\frac{p-2}{p-1} \right)^2 (1+z) \epsilon_{B,-1}^2 \epsilon_{e,-1}^2 n_0 E_{55} (1+Y)^2 \text{ s} \quad (\text{A-15})$$

Now we have listed the set of break frequencies for the SSC component. The SSC break frequencies are,

$$h\nu_{a,\text{ssc,fast}} = 2.41 \left[\frac{(p+2)(p-1)}{3p+2} \right]^{3/5} (1+z)^{-3/4} \epsilon_{B,-1}^{-4/5} n_0^{-3/20} E_{55}^{-1/20} t_2^{-1/4} (1+Y)^{-1} \text{ keV} \quad (\text{A-16})$$

$$h\nu_{a,\text{ssc,slow}} = 0.214 \left[\frac{(p+2)^{3/5} (p-1)^{-2/5} (p-2)}{(3p+2)^{3/5}} \right] (1+z)^{-1/4} \epsilon_{B,-1}^{1/5} \epsilon_{e,-1} n_0^{7/20} E_{55}^{9/20} t_2^{-3/4} \text{ MeV} \quad (\text{A-17})$$

$$h\nu_{c,ssc} = 0.328 (1+z)^{-3/4} \epsilon_{B,-1}^{-7/2} n_0^{-9/4} E_{55}^{-5/4} t_2^{-1/4} (1+Y)^{-4} \text{ MeV} \quad (\text{A-18})$$

$$h\nu_{m,ssc} = 18.1 \left(\frac{p-2}{p-1} \right)^4 (1+z)^{5/4} \epsilon_{B,-1}^{1/2} \epsilon_{e,-1}^4 n_0^{-1/4} E_{55}^{3/4} t_2^{-9/4} \text{ TeV} \quad (\text{A-19})$$

The break times for minimum and cooling frequencies are defined as,

$$t_{c,ssc} = 1.16 \times 10^{24} (1+z)^{-3} \epsilon_{B,-1}^{-14} n_0^{-9} E_{55}^{-5} (1+Y)^{-16} \nu_{c,ssc,eV}^{-4} \text{ s} \quad (\text{A-20})$$

$$t_{m,ssc} = 7.87 \times 10^7 \left(\frac{p-2}{p-1} \right)^{16/9} (1+z)^{5/9} \epsilon_{B,-1}^{2/9} \epsilon_{e,-1}^{16/9} n_0^{-1/9} E_{55}^{1/3} \nu_{m,ssc,eV}^{-4/9} \text{ s} \quad (\text{A-21})$$

The maximum flux values for the synchrotron and SSC emission are,

$$f_{\nu,\max} = 8.22 (1+z)^{-1} \epsilon_{B,-1}^{1/2} n_0^{1/2} E_{55} d_{28}^{-2} \text{ Jy}. \quad (\text{A-22})$$

$$f_{\nu,\max,ssc} = 5.42 \times 10^{-6} (1+z)^{-5/4} \epsilon_{B,-1}^{1/2} n_0^{5/4} E_{55}^{5/4} t_2^{1/4} d_{28}^{-2} \text{ Jy}. \quad (\text{A-23})$$

Adiabatic blastwave into the wind medium

The parameters have the same physical meaning as for the expressions defined above.

$$\Gamma = 78.25 (1+z)^{1/4} A_\star^{-1/4} E_{55}^{1/4} t_2^{-1/4}. \quad (\text{A-24})$$

$$R = 1.47 \times 10^{17} (1+z)^{-1/2} A_\star^{-1/2} E_{55}^{1/2} t_2^{1/2} \text{ cm}. \quad (\text{A-25})$$

$$B' = 35.96 (1+z)^{3/4} \epsilon_{B,-1}^{1/2} A_\star^{3/4} E_{55}^{-1/4} t_2^{-3/4} \text{ G}. \quad (\text{A-26})$$

$$\gamma'_m = 1.44 \times 10^4 \left(\frac{p-2}{p-1} \right) (1+z)^{1/4} \epsilon_{e,-1} A_\star^{-1/4} E_{55}^{1/4} t_2^{-1/4} \quad (\text{A-27})$$

$$\gamma'_c = 76.41 (1+z)^{-3/4} \epsilon_{B,-1}^{-1} A_\star^{-5/4} E_{55}^{1/4} t_2^{3/4} (1+Y)^{-1} \quad (\text{A-28})$$

$$\gamma'_s = 6.15 \times 10^6 (1+z)^{-3/8} \epsilon_{B,-1}^{-1/4} \phi_1^{-1/2} A_\star^{-3/8} E_{55}^{1/8} t_2^{3/8} (1+Y)^{-1/2} \quad (\text{A-29})$$

$$h\nu_{a,\text{fast}} = 0.15 \left[\frac{(p-1)(p+2)}{(3p+2)} \right]^{3/5} (1+z)^{3/5} \epsilon_{B,-1}^{6/5} A_\star^{11/5} E_{55}^{-2/5} t_2^{-8/5} (1+Y) \text{ eV}. \quad (\text{A-30})$$

$$h\nu_{a,\text{slow}} = 0.00081 \frac{(p-1)^{8/5} (p+2)^{3/5}}{(3p+2)^{3/5} (p-2)} (1+z)^{-2/5} \epsilon_{B,-1}^{1/5} \epsilon_{e,-1}^{-1} A_\star^{6/5} E_{55}^{-2/5} t_2^{-3/5} \text{ eV}. \quad (\text{A-31})$$

$$h\nu_c = 0.29 (1+z)^{-3/2} \epsilon_{B,-1}^{-3/2} A_\star^{-2} E_{55}^{1/2} t_2^{1/2} (1+Y)^{-2} \text{ eV}. \quad (\text{A-32})$$

$$h\nu_m = 1.01 \times 10^4 \left(\frac{p-2}{p-1} \right)^2 (1+z)^{1/2} \epsilon_{B,-1}^{1/2} \epsilon_{e,-1}^2 E_{55}^{1/2} t_2^{-3/2} \text{ eV}. \quad (\text{A-33})$$

$$h\nu_s = 1.85 (1+z)^{-3/4} \phi_1^{-1} A_\star^{-1/4} E_{55}^{1/4} t_2^{-1/4} (1+Y)^{-1} \text{ GeV}. \quad (\text{A-34})$$

$$t_c = 1.21 \times 10^3 (1+z)^3 \epsilon_{B,-1}^3 A_\star^4 E_{55}^{-1} (1+Y)^4 \nu_{c,eV}^2 \text{ s} \quad (\text{A-35})$$

$$t_m = 4.67 \times 10^4 \left(\frac{p-2}{p-1} \right)^{4/3} (1+z)^{1/3} \epsilon_{B,-1}^{1/3} \epsilon_{e,-1}^{4/3} E_{55}^{1/3} \nu_{m,eV}^{-2/3} \text{ s} \quad (\text{A-36})$$

$$t_0 = 1.88 \times 10^4 \left(\frac{p-2}{p-1} \right) (1+z) \epsilon_{B,-1} \epsilon_{e,-1} A_\star \text{ s} \quad (\text{A-37})$$

$$t_0^{\text{IC}} = 1.88 \times 10^4 \left(\frac{p-2}{p-1} \right) (1+z) \epsilon_{B,-1} \epsilon_{e,-1} A_\star (1+Y) \text{ s} \quad (\text{A-38})$$

$$h\nu_{a,ssc,\text{fast}} = 1.77 \left[\frac{(p+2)(p-1)}{3p+2} \right]^{3/5} (1+z)^{9/10} \epsilon_{B,-1}^{-4/5} A_\star^{-3/10} E_{55}^{1/10} t_2^{-1/10} (1+Y)^{-1} \text{ keV}. \quad (\text{A-39})$$

$$h\nu_{a,ssc,\text{slow}} = 0.33 \frac{(p-2)(p+2)^{3/5}}{(3p+2)^{3/5}(p-1)^{2/5}} (1+z)^{1/10} \epsilon_{B,-1}^{1/5} \epsilon_{e,-1} A_\star^{7/10} E_{55}^{1/10} t_2^{-11/10} \text{ MeV}. \quad (\text{A-40})$$

$$h\nu_{c,ssc} = 3.34 (1+z)^{-3} \epsilon_{B,-1}^{-7/2} A_\star^{-9/2} E_{55} t_2^2 (1+Y)^{-4} \text{ keV}. \quad (\text{A-41})$$

$$h\nu_{m,ssc} = 4.17 \left(\frac{p-2}{p-1} \right)^4 (1+z) \epsilon_{B,-1}^{1/2} \epsilon_{e,-1}^4 E_{55} A_\star^{-1/2} t_2^{-2} \text{ TeV}. \quad (\text{A-42})$$

$$t_{c,ssc} = 1.1 \times 10^{-7} (1+z)^{3/2} \epsilon_{B,-1}^{7/4} A_\star^{9/4} E_{55}^{-1/2} (1+Y)^2 \nu_{c,ssc,\text{eV}}^{1/2} \text{ s}. \quad (\text{A-43})$$

$$t_{m,ssc} = 2.04 \times 10^8 \left(\frac{p-2}{p-1} \right)^2 (1+z)^{1/2} \epsilon_{B,-1}^{1/4} \epsilon_{e,-1}^2 E_{55}^{1/2} \nu_{m,ssc,\text{eV}}^{-1/2} \text{ s} \quad (\text{A-44})$$

$$f_{\nu,\text{max}} = 10.44 (1+z)^{-1/2} \epsilon_{B,-1}^{1/2} A_\star E_{55}^{1/2} t_2^{-1/2} d_{28}^{-2} \text{ Jy}. \quad (\text{A-45})$$

$$f_{\nu,\text{max},ssc} = 3.81 \times 10^{-5} \epsilon_{B,-1}^{1/2} A_\star^{5/2} t_2^{-1} d_{28}^{-2} \text{ Jy}. \quad (\text{A-46})$$